FULL PAPER

Seismic wave attenuation (1/*Qp*) in the crust underneath the Eastern and eastern Southern Alps (Europe): imaging effects of faults, fractures, and fluids

Azam Jozi Najafabadi[1,2]*, Christian Haberland[1], Mark R. Handy[3], Eline Le Breton[3] and Michael Weber[1]

Abstract

We present a novel three-dimensional model of compressional wave attenuation (1/Q_P) for the Eastern and eastern Southern Alps in Europe that includes the eastern part of the Adriatic indenter, termed here the Dolomites Sub-Indenter. Our approach employed waveform data from the SWATH-D network, a dense temporary network operational between 2017 and 2019, as well as selected stations of the larger AlpArray Seismic Network. A spectral inversion method using frequency-independent quality factor Q_P, was applied to derive 3578 path-averaged attenuation values (*t**) from 126 local earthquakes. These were then inverted using the damped least square inversion (local earthquake tomography) for the attenuation structure. The resulting Q_P model, which builds on and complements a previously calculated 3-D velocity model (V_P and V_P/V_S), exhibits good resolution down to ~20 km depth. Several anomalies can be correlated with the distribution of other physical parameters (V_P and V_P/V_S) and regional tectonic features. Notably, the Friuli-Venetian region exhibits the highest attenuation (lowest Q_P) anomaly, coinciding with low V_P values and increased V_P/V_S. This anomaly is likely associated with a high density of faults and fractures, as well as the presence of fluid-filled sediments along the active thrust front in the eastern segment of the Southern Alps. Another intriguing observation is the low attenuation (high Q_P) anomaly along the northwestern edge of the Dolomites Sub-Indenter (NWDI), located south of the Periadriatic fault and east of the Giudicarie fault, where seismicity is notably absent. This anomaly coincides with Permian magmatic rocks at the surface and may be a measure of their strength at depth.

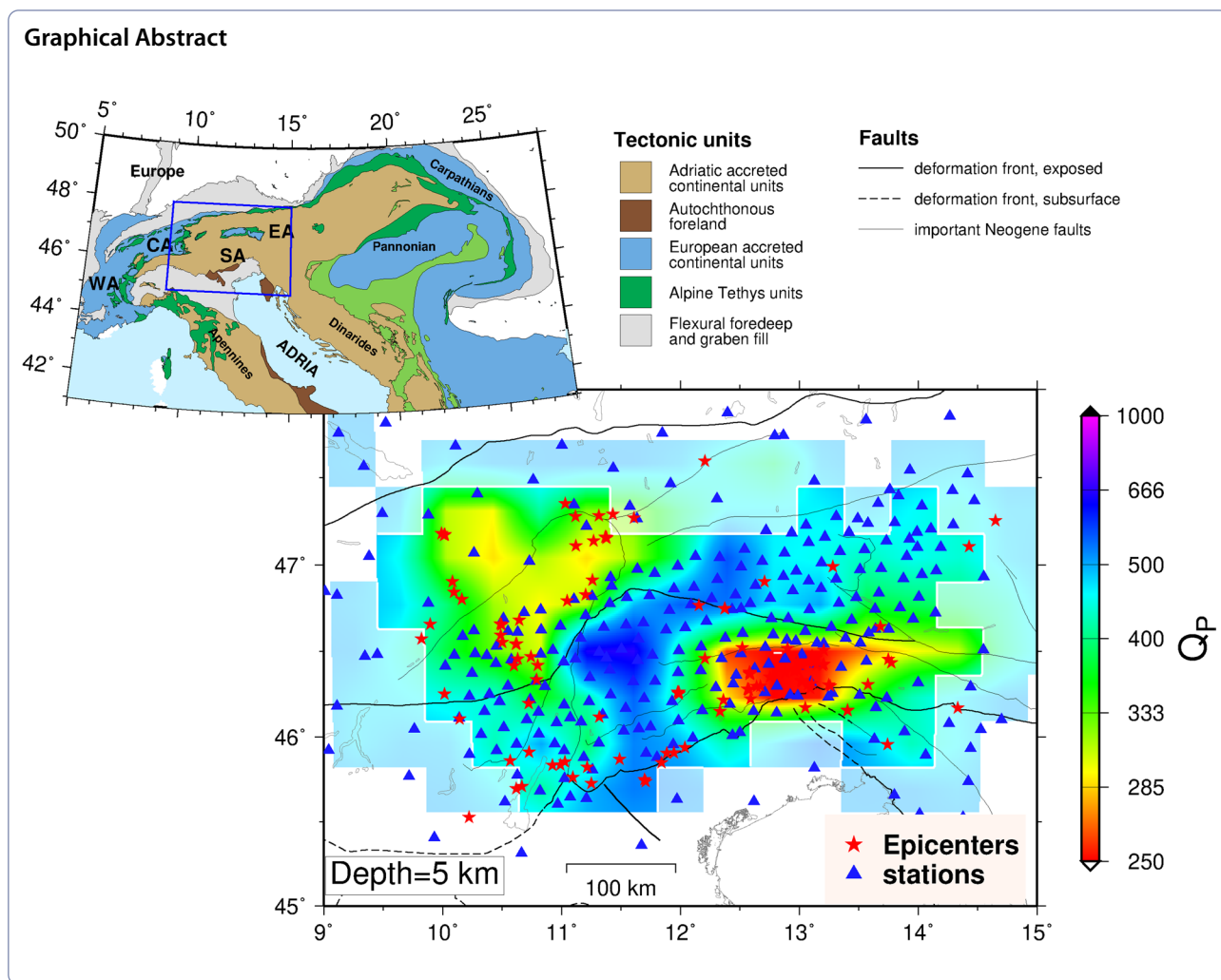**Keywords** Alpine orogeny, Crustal structure, Seismic attenuation, Seismic tomography, Body waves

*Correspondence:
Azam Jozi Najafabadi
azam@gfz-potsdam.de
Full list of author information is available at the end of the article

Jozi Najafabadi *et al. Earth, Planets and Space*   (2023) 75:187

Page 2 of 15

Graphical Abstract

Introduction

Seismic attenuation (expressed by the inverse of the seismic quality factor Q) is the energy loss of seismic waves when passing through a medium (Aki and Richard 1980). This happens when the energy is dissipated as heat and/or as inelastic (plastic and/or viscous) deformation. Attenuation can be attributed to a variety of mechanisms, for example, the motion of fluids in pores and fractures of fluid-filled rocks (Eberhart-Phillips 2016), melt coating grain boundaries, and/or dislocations within grains and grain aggregates at sufficiently high temperatures (Mavko et al. 2020). Therefore, attenuation is not just diagnostic of a certain lithology, it is also sensitive to the physical conditions and state of the rocks. It is hence complementary, for example, to seismic velocities or the Poisson ratio. Furthermore, scattering can significantly contribute to the attenuation of seismic waves.

Since seismic attenuation is highly sensitive to the presence of fluids, high temperature, and melt, it has been used for investigating volcanoes (Lin et al. 2015), geothermal fields (Muksin et al. 2013), and subduction zones (Haberland and Rietbrock 2001; Bohm et al. 2013). It has also proved useful for investigating sedimentary basins (Hauksson and Shearer 2006; Bohm et al. 2013) and earthquake source zones (Rietbrock 2001; Wang et al. 2017).

In this paper, we investigate the attenuation of seismic (body) P-waves in the crust of the Eastern and eastern Southern Alps (Europe) in order to shed light on the crustal structure and processes involved in the Alpine orogeny. Attenuation studies (in particular attenuation tomography) are sparse in the Alps. The large-scale study by Mayor et al. (2016) found strong lateral variability of absorption (coda Q) across the entire Alps, with length scales ranging from 100 to 1000 km. Campillo et al. (1993) found anomalous propagation of *Lg* waves in the Western Alps. Several studies reported elevated attenuation (engineering parameter kappa, amplitudes, coda Q)

Jozi Najafabadi *et al. Earth, Planets and Space* (2023) 75:187

Page 3 of 15

in northeastern Italy (Castro et al. 1996; Morasca et al. 2010; Gentili and Franceschina 2011; Gentili and Gentile 2015). Recently, Lanza et al. (2021) derived a 3-D model of the attenuation ($1/Q_P$ and $1/Q_S$) of the central Alps and their forelands.

Here, we use data observed by the dense, temporary SWATH-D network (Heit et al. 2017; 2021) deployed in the Eastern and eastern Southern Alps from 2017 to 2019 and complemented by data of selected stations of the AlpArray network (Hetényi et al. 2018). In particular, we used observations of local earthquakes from Jozi Najafabadi et al. (2022), in which 3-D models of V_P and Poisson's ratio of the crust and uppermost mantle were derived.

The study focuses on a specific region within the Alpine chain, which was formed during indentation of the northern tip of the Adriatic Plate (Adriatic indenter; AI) into the European Plate in Oligo-Miocene time (Schmid et al. 2004; Handy et al. 2010; Le Breton et al. 2021). The Dolomites Sub-Indenter, defined as the part of the AI located east of the Giudicarie fault (GF) and between the Periadriatic fault (PAF) in the north and the Southern Alpine deformation front in the south, is one of the key structures in our target area (Fig. 1). The PAF is a major dextral strike-slip fault active in Oligo–Miocene

time that separates the Eastern from the Southern Alps (Schmid et al. 1989; Handy et al. 2015). The Northern Giudicarie fault is a sinistral strike-slip fault that separates the eastern Southern Alps in the east from the Austroalpine nappes in the west (Castellarin et al. 2006; Pomella et al. 2011, 2012; Verwater et al. 2021). Deformation of the Dolomites Sub-Indenter involved predominantly south-directed folding and thrusting in the eastern Southern Alps since early-mid Miocene time (Castellarin et al. 1987; Castellarin and Cantelli 2000; Reiter et al. 2018) and continues to the present (Serpelloni et al. 2016; Sánchez et al. 2018). This fold-and-thrust belt affects the Mesozoic sedimentary cover and Permian magmatic rocks (e.g., Castellarin et al. 2006 and refs. therein; Tadiello and Braitenberg 2021).

The seismicity in the region is distributed in diffuse clusters and is localized mostly in the orogenic retrowedge comprising the nappes of the Southern Alps in the Friuli-Venetian region (FV) and the Giudicarie Belt. Additionally, seismic activity is seen in the Austroalpine nappes located north of the PAF. Regions with limited or no activity are found at the northwestern edge of the Dolomites Sub-Indenter (NWDI) and further north of the PAF. The overall seismicity pattern is a reflection of the head-on convergence of the Adriatic indenter with
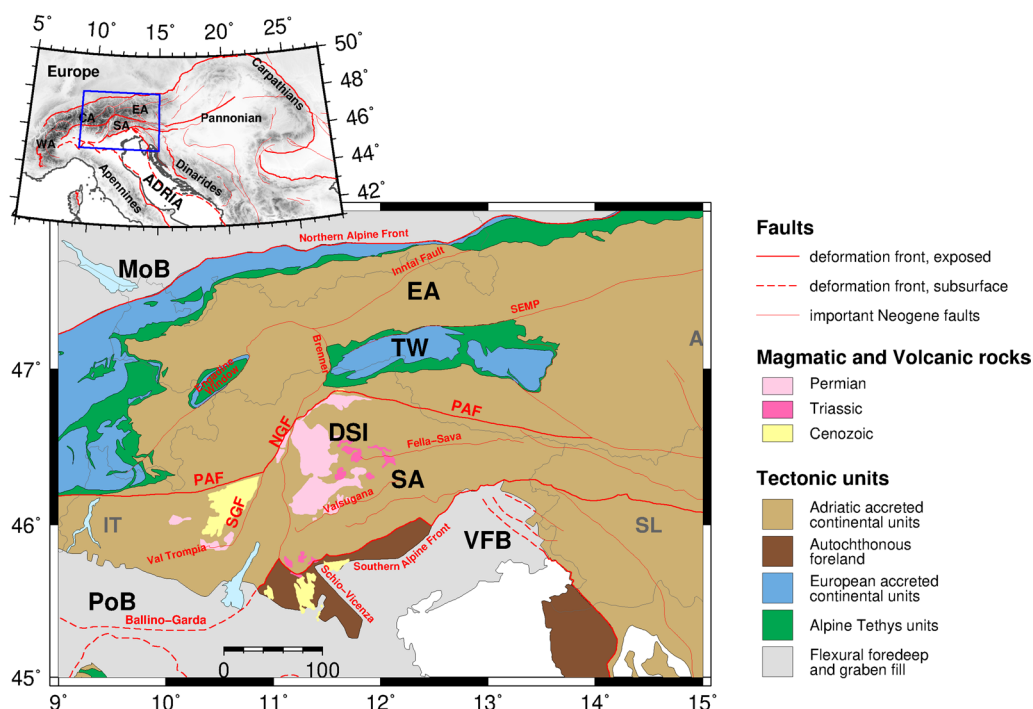

Fig. 1 Tectonic map of the region showing faults, geographical subdivisions, and tectonic units modified after Schmid et al. (2004, 2008) and from M. R. Handy based on sources listed in Handy et al. (2019). *CA* Central Alps, *DSI* Dolomites sub-indenter, *EA* Eastern Alps, *MoB* Molasse Basin, *NGF* Northern Giudicarie fault, *PAF* Periadriatic fault, *PoB* Po Basin, *SA* Southern Alps, *SEMP* Salzach-Ennstal-Mariazell-Puchberg, *SGF* Southern Giudicarie fault, *TW* Tauern Window, *VFB* Venetian-Friuli Basin, *WA* Western Alps, *IT* Italy, *SL* Slovenia, *AT* Austria

Jozi Najafabadi *et al. Earth, Planets and Space*   (2023) 75:187

Page 4 of 15

the Alpine orogenic crust. This convergence is accommodated through thrust faults and folds in the FV region and is segmented in the NWDI by strike-slip faults of the Giudicarie Belt (Jozi Najafabadi et al. 2021, 2022; Hofman et al. 2023; Reiter et al. 2018).

The objective of this study is to investigate the tectonic structure in the Eastern and eastern Southern Alps by observing seismic attenuation anomalies in P-waves and exploring their possible connection to seismic activity.

Data and attenuation estimation methodology

In this study, we use data from 499 well-constrained local earthquakes between September 2017 and November 2019. The waveform data were recorded by 161 seismic stations of the temporary local SWATH-D network (Heit et al. 2017, 2021) and 112 selected stations of the larger scale AlpArray Seismic Network (AASN; Hetényi et al. 2018) (Fig. 2). We selected only stations with sampling rates of 100 or 200 samples per second (sps). Waveform data of the stations with a sampling rate of 200 sps were down-sampled to 100 sps.

The P- and S-wave arrivals of this local earthquake catalog were manually picked, and the hypocenters were determined using a simultaneous inversion for the 3-D velocity structure and earthquake parameters (Jozi Najafabadi et al. 2022). In the dataset, we noticed pronounced direct Pg, Moho-reflected PmP, and Moho-refracted Pn waves which arrive closely spaced in time (around the critical distance). Therefore, to avoid misidentification of three types of P phases, we excluded any first arrivals that may not correspond to the Pg. To achieve this, we employed the concept of the cross-over distance, which is determined by equating the travel times of Pg and Pn waves within a simplified two-layer velocity model (resembling crust and mantle). The cross-over distance depends on the velocity of the crust and mantle (taken from Jozi Najafabadi et al. 2021), as well as earthquake and Moho depth. For the attenuation tomography, we utilized only picks that have an epicentral distance smaller than the cross-over distance. However, our dataset includes only a small number of picks at an epicentral distance larger than the cross-over distance and the results look similar with or without considering these picks.

On each waveform (vertical component), first, a 2.56-s window around the P-wave onset was selected and the baseline was removed, then the signal spectrum was calculated using the multi-taper approach (Park et al. 1987). For calculating the noise spectrum, a time window of the same length was selected preceding the selected P-wave window and the spectrum calculated as before (upper panels of Fig. 3). The observed P spectrum at the station i related to the ray path coming from the source j is affected by the source spectrum, instrument response, receiver site effect, geometrical spreading, and attenuation (Scherbaum 1990; Sanders et al. 1993). After correction for instrument response and assuming a Brune source spectrum (Brune 1970,
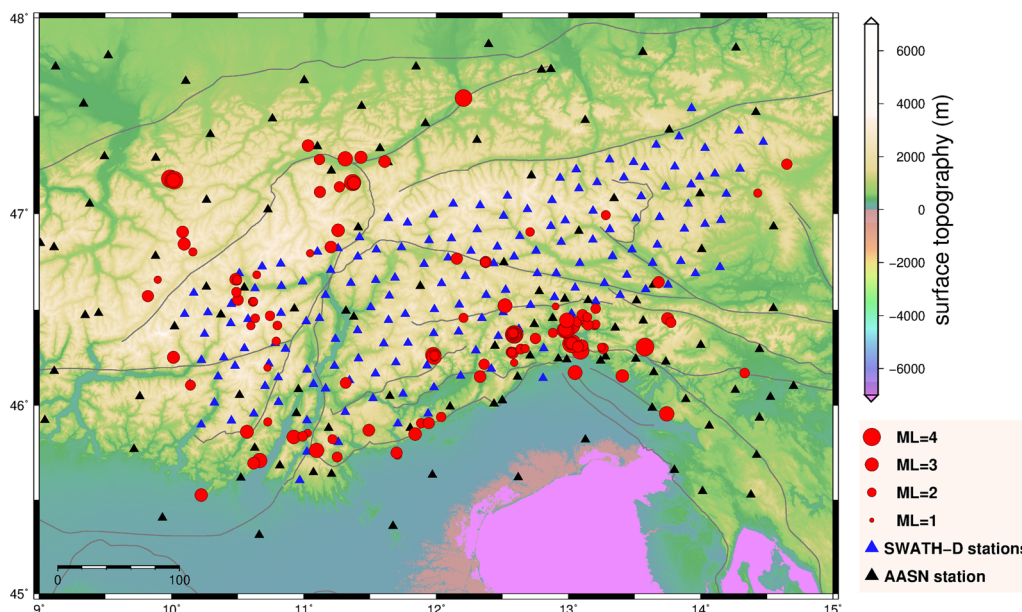

Fig. 2 Distribution of seismic stations of the SWATH-D network (blue triangles) and selected stations of the AASN (black triangles). Red circles indicate the epicenters of local earthquakes used in attenuation tomography. The faults are from Handy et al. (2010, 2019) and Schmid et al. (2004, 2008)
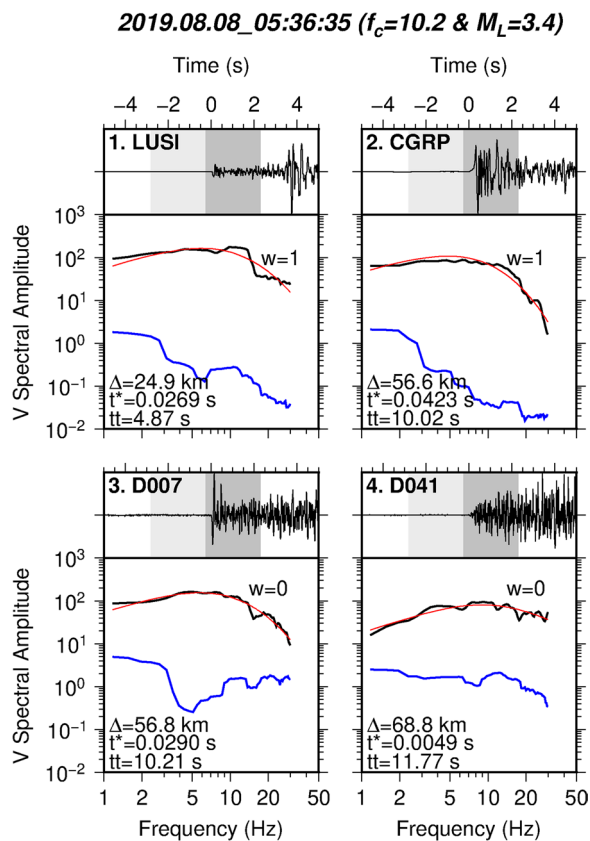
Jozi Najafabadi *et al. Earth, Planets and Space*   (2023) 75:187

Page 5 of 15

2019.08.08_05:36:35 (f_c=10.2 & M_L=3.4)

Fig. 3 Examples of the noise (blue line), observed P signal (black line), and modeled (red line) spectra for four stations LUSI, CGRP, D007, and D041 of an event with M_L = 3.4. In the upper panels, the normalized time series waveforms and the selected 2.56 s windows for analyses of signal and noise (dark and light gray, respectively) are displayed. t^*, tt, f_c, Δ, and w are the whole path attenuation, travel-time, source corner frequency, epicentral distance, and weight (representative of the quality of the signal), respectively. The comparison of the four stations shows how the slope and shape of the P signal spectrum affect the t^* value and the quality weight

1971; Hanks and Wyss 1972), the amplitude spectra can be described by:

$$A_{ij}(f) = \frac{\Omega'_{0ij}\exp\left(\pi f t^*_{ij}\right)}{1 + \left(\frac{f}{f_{cj}}\right)^2}, \quad (1)$$

where f is the frequency, Ω'_{0ij} is the signal moment (taking up all frequency-independent factors, such as spectral moment, instrument gain, site amplification, and geometrical spreading), f_{cj} is the corner frequency (common for all observations of an event), and t^*_{ij} is the whole path attenuation. A nonlinear spectral inversion is then performed to determine the free parameters Ω'_{0ij}, f_{cj} and t^*_{ij} by minimizing the difference between observed and modeled spectra (Rietbrock 2001; Haberland and Rietbrock 2001; Eberhart-Phillips and Chadwick 2002).

The following criteria have been chosen for including an observation (signal spectrum) in the spectral inversion: (1) minimum signal-to-noise ratio of 1.4 over the frequency band 1–30 Hz; (2) minimum epicentral distance of 20 km; and (3) minimum travel-times of 3.5 s. The first criterion is for considering only signals with sufficient energy and the last two ones prevent contamination of the P spectrum with S-wave signal. Moreover, only events with at least nine t^* were utilized for the inversion. Considering these constraints, we could derive 3578 t^* values in the epicentral distance between 20 and 200 km from 126 local earthquakes in the depth range of 0 and 20 km and M_L range of 1 and 4.2 (epicenters are shown in Fig. 2).

The t^*_{ij} values are then weighted based on the misfit between the observed and modeled spectra. Only continuous portions of signal spectra with a frequency band between 1 and 10–30 Hz (spectral amplitude must be 1.4 times above the noise spectrum) were included in the spectral inversion. Figure 3 illustrates the signal and noise spectral analyses for 4 stations of an event with M_L = 3.4 as an example. In this figure, the resemblance of the noise, observed and modeled signal spectra are illustrated with blue, black, and red lines, respectively. The poor spectral fit and therefore higher weight (e.g., station LUSI) is most likely due to site effects which usually show up as characteristic distortions in the observed spectra.

In order to estimate the uncertainty of the t^* values, we analyzed the similar ray paths that originated from closely spaced sources and recorded in the same station. For the similar rays, it is expected to derive similar t^* values (as they share similar paths) and different f_c (as they are produced by different events). We divided the region into 500 m×500 m×250 m cells. The t^* values that originated from different events within each cell (at least 2 events per cell) and were recorded at the same stations were considered for assessment of the uncertainties (a total number of 643 t^* values). Figure 4a shows the t^* values versus their averages along common ray paths and Fig. 4b demonstrates the histogram of t^* deviations from their averages. Both figures indicate that t^* values have a consistent standard deviation of ~0.015 s which can be representative of t^* uncertainty (comparable values have been found in similar studies, e.g., in Haberland and Rietbrock 2001). The relatively small standard deviation indicates that the inversion method successfully separates the source and path effects.

Attenuation tomography and model resolution

After analyses of the t^* values, the P-wave attenuation ($1/Q_P$) along the ray paths can be calculated using the following formulation:
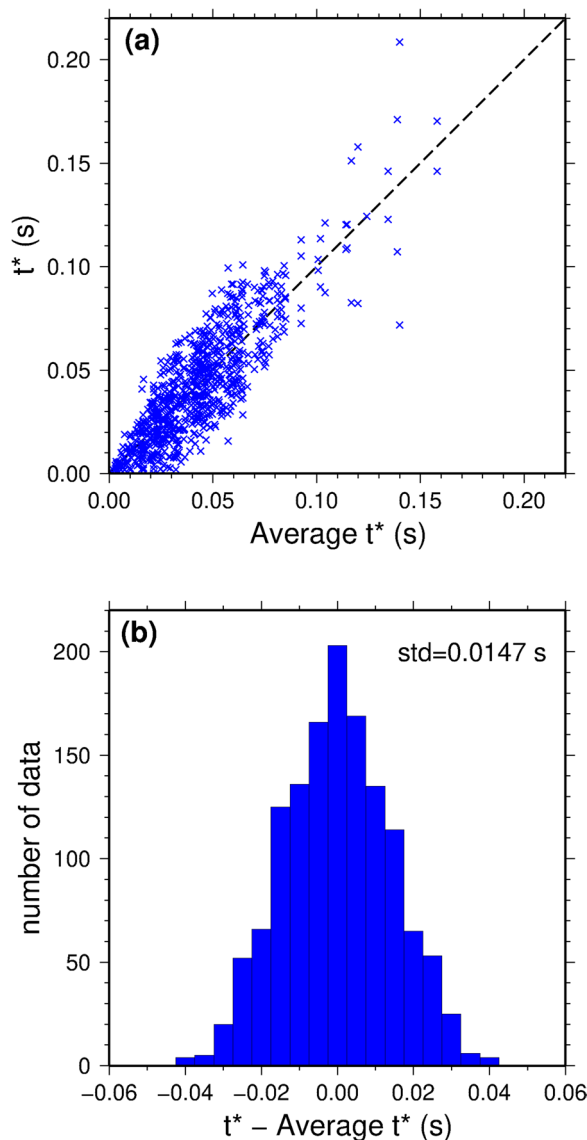
Jozi Najafabadi *et al. Earth, Planets and Space*   (2023) 75:187

Page 6 of 15

Fig. 4 The assessment of the t^* uncertainty by comparison of the t^* values of similar ray paths. **a** The t^* values versus their averages along common ray paths. **b** The histogram of t^* deviations from their averages along common ray paths. The standard deviation of ~0.015 is assumed to be the t^* uncertainty

$$t_{ij}^* = t_0^* + \int Q_P^{-1}(x,y,z) V_P^{-1}(x,y,z) dr, \qquad (2)$$

where t_0^* is a constant accounting for the local site effect (so-called station correction), V_P is the 3-D P-wave velocity model, and dr is an element along the ray path.

Once the t^* values of all source–receiver ray paths are determined, they are inverted for a 3-D Q_P image using the well-established SIMUL2000 algorithm (Thurber 1983; Eberhart-Phillips and Michael 1993; Evans et al.

1994). This code uses an iterative damped least square method and requires a 3-D seismic grid with initial Q_P and already determined V_P values associated with the nodes. The values between the grid nodes are linearly interpolated (Thurber 1983). The solution to the forward problem (ray path calculation) is accomplished using a combination of approximate ray tracing (Thurber 1983) and a pseudo-bending scheme (Um and Thurber 1987).

The earthquake hypocenters, origin-times, and three-dimensional velocity model (V_P) of this dataset are taken from Jozi Najafabadi et al. (2022) which were determined using 16,484 P and 9554 S travel-time records of 499 local earthquakes in a nonlinear velocity tomographic inversion. We initiated the inversion with a homogeneous Q_P model using the starting value of 550 which yields a balanced distribution of high and low Q_P anomalies throughout the studied volume. Since the tomographic solutions strongly depend on the choice of initial parameters (Kissling et al. 1994), we performed the inversion with a wide range of initial Q_P values (between 100 and 1000). The resulting 3-D models demonstrate a very similar pattern of anomalies and only the amplitude of anomalies changes.

Model parametrization and regularization are two other key parameters in the tomographic inversions. The parametrization should provide a compromise between the resolution and robustness. After testing various grid sizes and considering the number of available t^* values, stations, and earthquakes, we considered the same (coarse) grid of the travel-time tomography (V_P and V_P/V_S; Jozi Najafabadi et al. 2022). This 3-D model grid was centered on the midpoint of the study area (12°E and 46.5°N) with 30 km×30 km horizontal node spacing. The vertical layers are placed at depths of − 5, 0, 5, 10, 20, 30, 45, 60, and 90 km.

In order to select a proper damping value (regularization) and stabilize the inversion process, a series of single-iteration inversions using a wide range of values were performed. The optimal value was then selected based on the so-called trade-off curve between the data variance and model variance (Eberhart-Phillips 1986) as 0.02.

Having finalized the inversion process, the quality of the tomographic models should be evaluated through analysis of the model resolution matrix (MRM; Eberhart-Phillips and Michael 1993) and synthetic tests. In this study, we first calculated the spread function (Toomey and Foulger 1989) which translates the information in each row of the MRM into a single value and describes the resolution of the individual nodes.

The spread function represents the resolution of the final Q_P model. Low values indicate high resolution, whereas high values imply lower resolution. The

Jozi Najafabadi *et al. Earth, Planets and Space*   (2023) 75:187

Page 7 of 15

resolution (spread value) distribution is strongly influenced by the crossing ray paths and it is dominated by the geometry of the earthquakes and stations. The seismicity in our study area is restricted to the uppermost 20 km of the crust and is mostly located within the upper 10 km depth. Therefore, the best resolution is observed down to 20 km. Below 20 km depth, due to the removal of arrivals after the cross-over distance (see above), little resolution is expected. By comparison of the ray coverage and spread value geometries and also considering the recovery of the synthetic tests (see following), the spread value of 3.4 proved to be a reasonable threshold that fairly separates well from poorly resolved regions.

The spread values of the final Q_P model are illustrated for 4 depth slices in Fig. 5a. The depth slices show that the spread values in the middle of the region from the surface down to the depth of 20 km are quite low (< 3) and the resolution is high. The region outside the spread threshold (white line) is moderately resolved.

In order to complement the resolution assessment, we perform two commonly used synthetic tests in tomography studies. In both tests, the background model ($Q_P = 550$) is perturbed by high and low anomalies ($\pm 50\%$) and synthetic t^* values are calculated using the forward solution of the SIMUL2000 code for the same source–receiver distribution. For resembling similar conditions as the real data inversion, Gaussian noise with a standard deviation equivalent to t^* uncertainty of the real data (0.015 s; Fig. 4b) is added to the synthetic t^* values. Thereafter, the inversion of the synthetic t^* values is performed using the uniform background Q_P model. These tests provide information on the recovery of the random Q_P anomalies with different sizes.

The first synthetic test is performed using the classical checkerboard model, in which the background model is perturbed by low and high anomalies through 2×2 lateral grid nodes at depths of 0 and 10 km with swapped polarities. The nodes between the alternating anomalies are left unperturbed. The purpose of a checkerboard test is to add further information about spatial smearing to the model resolution. Figure 5b shows the recovery of the checkerboard test through 4 horizontal slices. The blocks located in the central volume of the region at depths of 0 and 10 are recovered very well with minor lateral smearing. The vertical smearing is larger at the depth slices of 5 and 20 km, which were left unperturbed in the checkerboard model. The geometry of the well-recovered area is very similar to the area with a spread value below 3.4 (Fig. 5a).

The second synthetic test was performed using the so-called characteristic model which works with a similar principle as the checkerboard test. The anomalies in the characteristic model test are inspired by the anomalies

seen in the Q_P tomography of the real data. The purpose is to test whether features comparable to those observed in the real model are recoverable. In our test, one low attenuation anomaly in the NWDI and two highly attenuated anomalies (low Q_P), one in the FV region and one in the western part of the Austroalpine units (WAU; to the northwest of the NWDI), are placed at depth layers of 0, 5, and 10 km.

The results (Fig. 5c) show very good recovery of the anomaly in the FV at all three depth slices, however, at depths of 0 and 5 km horizontal smearing patches can be observed. The anomaly in the WAU is also recovered at all depth slices with negligible smearing, although the amplitude of this anomaly at depth of 10 km is reduced. The low attenuation anomaly in the NWDI is very well recovered at depths of 5 and 10 km with slight horizontal smearing, however, it is poorly recovered at depth of 0 km.

The conclusions of the synthetic tests, specifically the smearing effects, should be considered for the interpretation of the real data tomography.

Results

Q_P tomographic results are shown for four depth slices in Fig. 6a and four vertical cross sections in Fig. 7a, respectively. For comparison of the attenuation and velocity structures, the V_P and V_P/V_S models (Jozi Najafabadi et al. 2022) are included in the figures (Figs. 6b, 6c, 7b, and 7c) as well.

In the map views of Fig. 6a, increased attenuation ($Q_P < 300$) is found in the FV region from the surface down to a depth of 10 km (also Fig. 7a, cross sections A & D). Although the characteristic model test indicated smearing patches in the FV region, the Q_P results reveal a very pronounced and focused high-attenuation anomaly in this region. The highest attenuation in the whole study region ($Q_P \leq 250$) is located at a depth of 5 km in this zone. The V_P model (Figs. 6b and 7b) looks complex in this region and shows low values at depths of 5, 10, and 20 km, within which patches of higher values are observed. The V_P/V_S maps (Figs. 6c and 7c) reveal high values in this region. However, the high V_P/V_S anomaly is larger and extends further south into the Venetian-Friuli Basin. Moreover, a zone of increased earthquake activity corresponds to this region (more prominent in Figs. 6b and 7b). This has been the site of two destructive earthquakes in the past (May 6 and September 15 of 1976; Slejko 2018).

In the NWDI, low attenuation ($Q_P > 600$) is recorded, especially at a depth of 10 km. The V_P map reveals increased values (6–6.5 km/s) at depth slices of 10 and 20 km in this region. The V_P/V_S maps do not indicate any
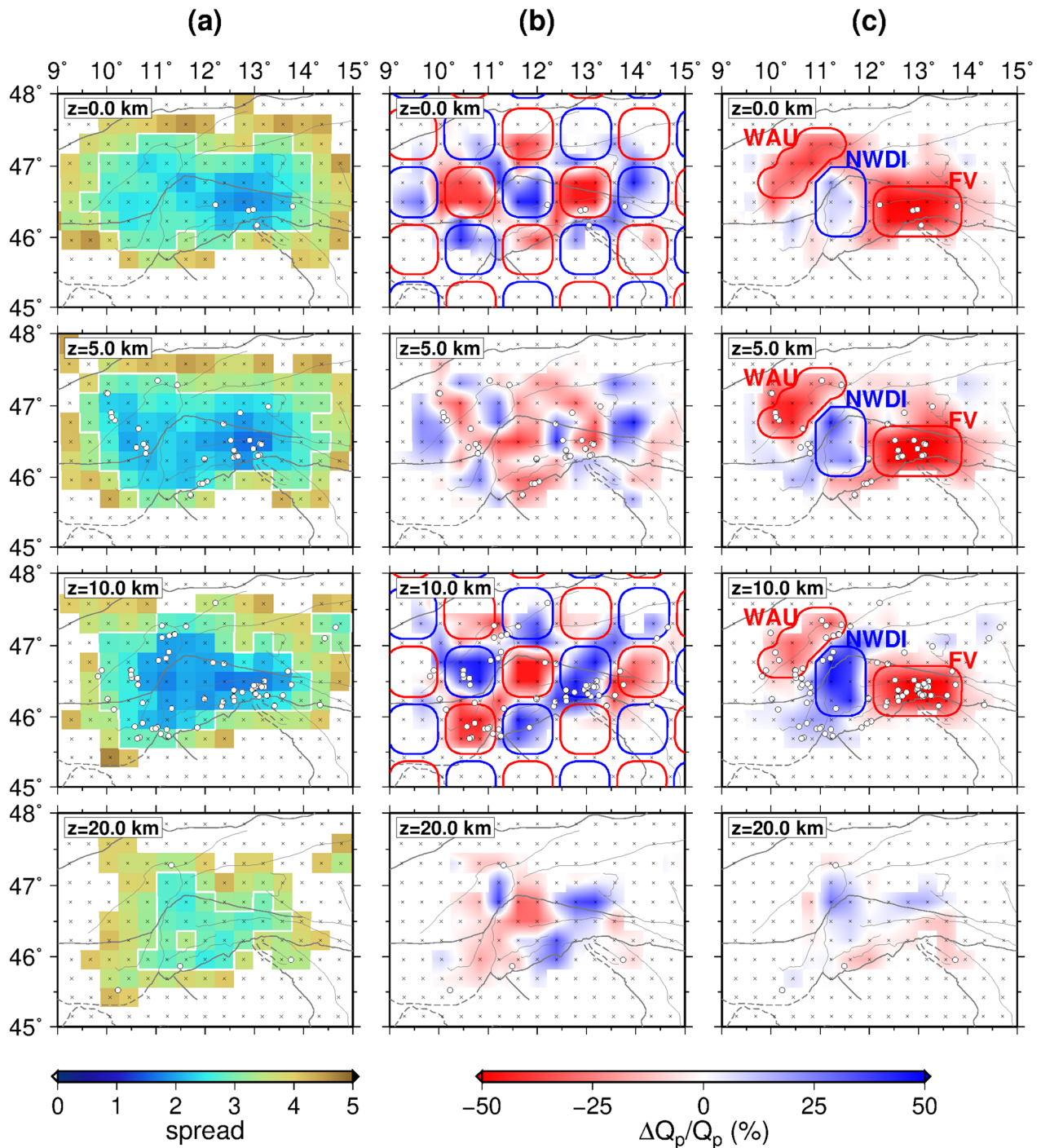
Fig. 5 **a** Spread values of the Q_P model through four depth slices. The unresolved regions (no ray coverage) are masked with white and the poorly resolved area is separated from the well-resolved area with a white solid line (spread value threshold of 3.4). **b** The recovery of the classical checkerboard test with alternating anomalies (±50% of the background model $Q_P = 550$) over four lateral nodes. **c** The recovery of the characteristic model test that is inspired by the Q_P anomalies (±50% of the background model $Q_P = 550$) of the real data. The high and low input anomalies in both checkerboard and characteristic models are indicated with blue and red squares, respectively. The black crosses and the white circles denote the grid nodes and hypocenters, respectively. *FV* Friuli-Venetian Region, *NWDI* Northwestern edge of dolomites sub-indenter, *WAU* Western part of the Austroalpine units
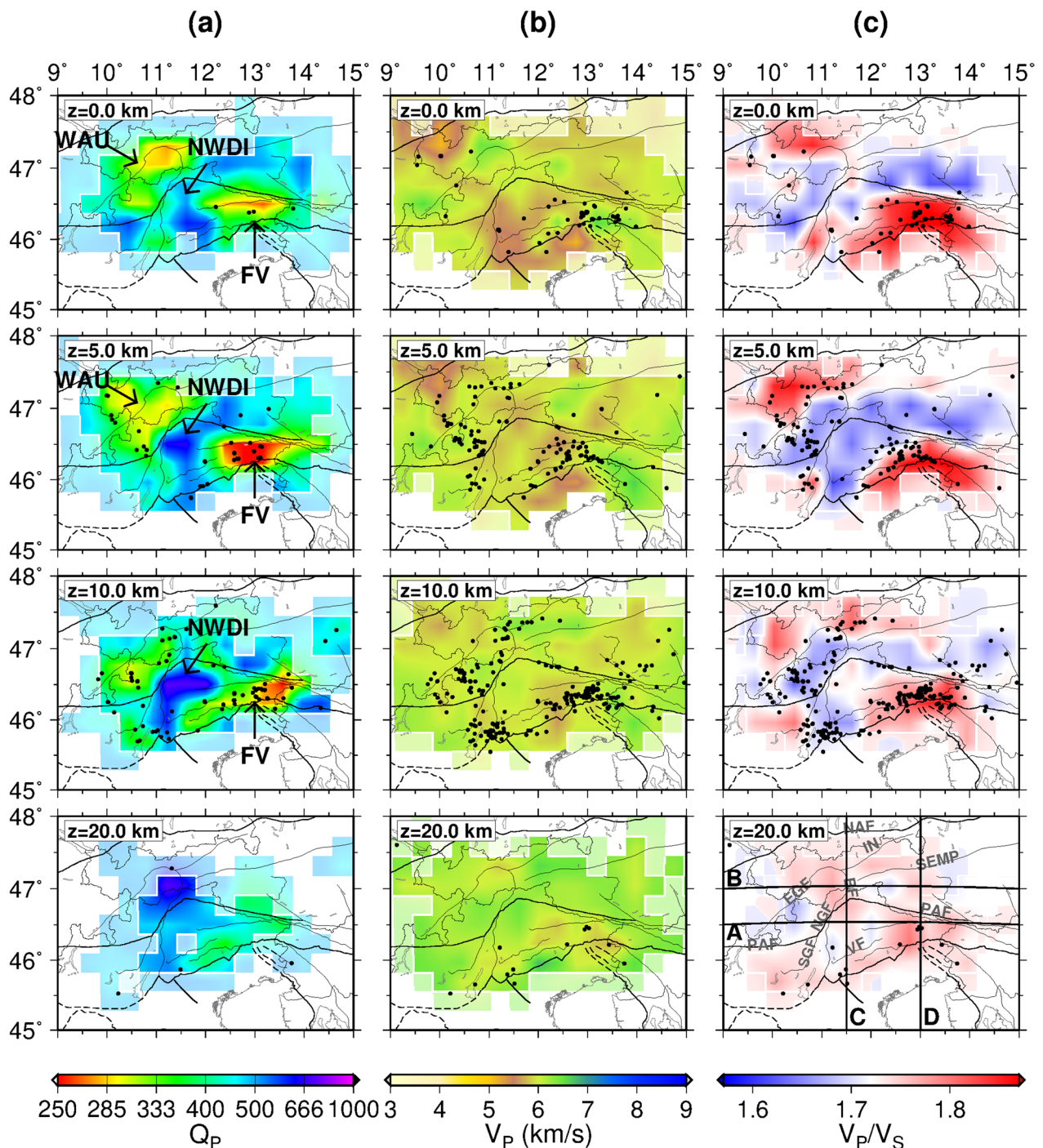
Fig. 6 The map view of **a** the attenuation structure ($1/Q_P$), **b** the V_P structure, and **c** the V_P/V_S structure at depths of 0, 5, 10, and 20 km. The V_P and V_P/V_S models are taken from Jozi Najafabadi et al. (2022). The black circles indicate epicenters of local earthquakes with $M_L \geq 1$ in the time frame between September 2017 and November 2019. *FV* Friuli-Venetian Region, *BF* Brenner Fault, *EGF* Engadin Fault, *IN* Inntal Fault, *NAF* Northern Alpine Front, *NGF* Northern Giudicarie fault, *NWDI* Northwestern edge of Dolomites Sub-Indenter, *PAF* Periadriatic fault, *SEMP* Salzach-Ennstal-Mariazell-Puchberg, *SGF* Southern Giudicarie fault, *VF* Valsugana Fault, *WAU* Western Part of Austroalpine units
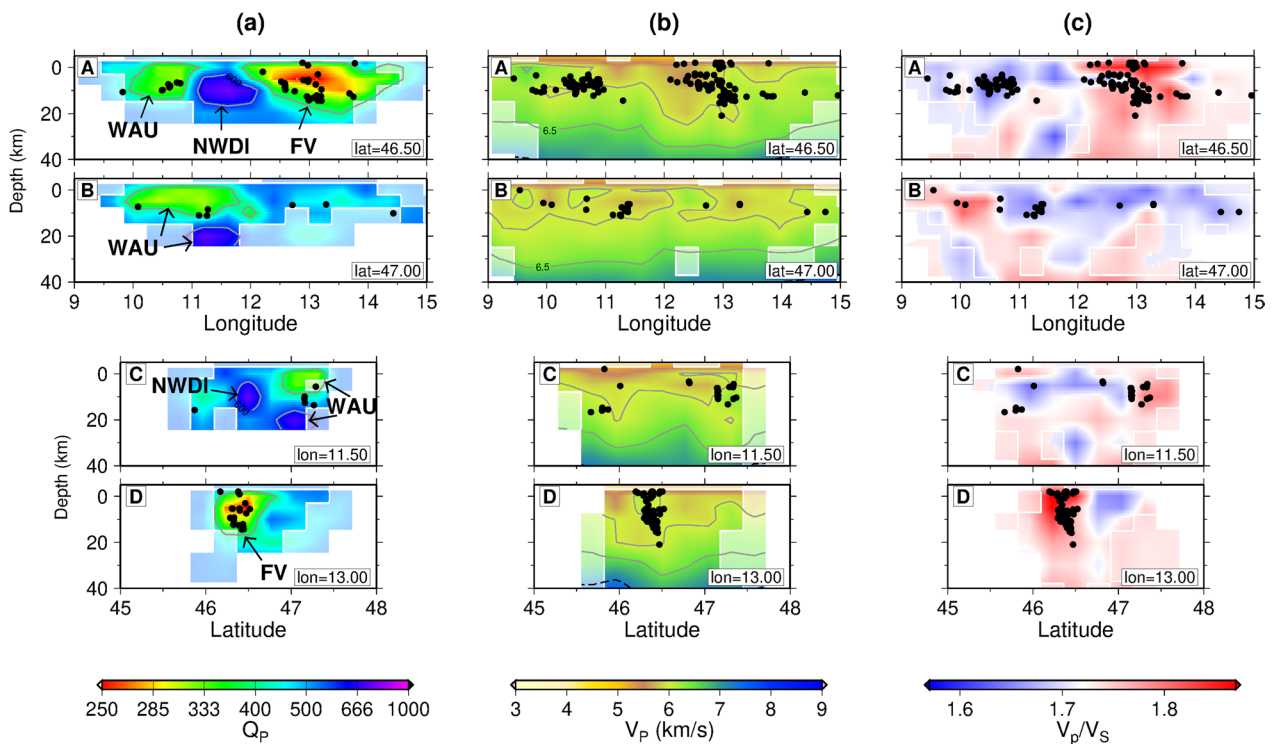
Fig. 7 Vertical cross sections of **a** the attenuation structure ($1/Q_P$), **b** the V_P structure, and **c** the V_P/V_S structure along profiles A, B, C, and D of Fig. 6c, depth slice of 20 km. The V_P and V_P/V_S models are taken from Jozi Najafabadi et al. (2022). The vertical exaggeration of all the cross sections is 3:1. The hypocenters projected from a swath extending to 15 km on either side of the profiles are shown with black circles. For abbreviations see the caption of Fig. 6

pronounced anomaly, although lower V_P/V_S values are registered here than in the FV region.

The WAU is also a domain of heightened attenuation ($Q_P \sim 300$). Its geometry changes with depth from the surface down to 10 km depth (Figs. 6a and 7a, cross sections B & C). At a depth of 20 km, attenuation decreases (Q_P increases to ~750) across the Brenner fault (Fig. 6a, depth slice of 20 km), albeit at reduced resolution (Fig. 5a). V_P shows a complex pattern in this region, with increased values from the surface down to a depth of 10 km, whereas reduced values are observed at a depth of 20 km (Fig. 6b). The V_P/V_S model shows some high values NW of the Engadin fault (Fig. 6c).

The three depth slices at 0, 5, and 10 km in Fig. 6a indicate that the Giudicarie fault is a noticeable boundary between the lower attenuation on its SE side and higher attenuation to the NW.

Discussion

We present a novel 3-D model of the specific seismic attenuation of body P-waves in the Eastern and eastern Southern Alps calculated using 3,578 path-average attenuation (t^*) values from 126 local earthquakes. The t^* dataset (and the number of usable earthquakes) is

much smaller than the travel-time dataset used for the calculation of the V_P model (22%). As a result, the Q_P 3-D model has a much coarser parameterization than the V_P model. This is mainly because the method to calculate t^* requires spectral observations with a high signal-to-noise ratio over a relatively large frequency range, which is not the case throughout our dataset dominated by small-magnitude earthquakes. Furthermore, t^* values are typically noisier. Finally, due to the limited number of observations at a larger distance, the lowermost crust and the mantle are only poorly resolved or unresolved. However, the attenuation model in Sect. "Results" reveals prominent attenuation anomalies in the crust that correlate with tectonic features in the study area.

Strongly elevated attenuation in the FV region (Figs. 6a and 7a) encompasses the eastern part of the Southern Alpine Front and reaches both north to the PAF and south to the northeasternmost part of the Venetian-Friuli Basin. The FV region is the seismically most active zone in the Alps, with active thrusts and back-thrusts (e.g., Nussbaum 2000; Galadini et al. 2005; Slejko 2018; Romano et al. 2019; Jozi Najafabadi et al. 2021). The Q_P resolution assessments show that the FV region is

Jozi Najafabadi *et al. Earth, Planets and Space*   (2023) 75:187

Page 11 of 15

reasonably well resolved, although minor lateral smearing is observed.

The zone of high attenuation in the FV region coincides largely with low V_P (~ 5.5 km/s) and high V_P/Vs (Figs. 6b, c, 7b and c), thus it coincides with low Vs. However, the high V_P/Vs region is much larger than the low Q_P region and encompasses more of the Venetian-Friuli Basin. Low Q_P is more concentrated along the eastern part of the Southern Alpine Front. Sadeghi-Bagherabadi et al. (2021) also illustrated a decrease in V_S values in close proximity to our highly attenuated FV anomaly. Furthermore, high attenuation of shear waves has been reported for this region (Gentili and Franceschina 2011).

Sedimentary basins are well known for their high attenuation (Li et al. 2006; Hauksson and Shearer 2006; Bohm et al. 2013; Muksin et al. 2013) probably due to fluids in pores and cracks, which when over-pressured, can significantly increase attenuation (see e.g., Peacock et al. 1994; Hauksson and Shearer 2006; Bohm et al. 2013; Mavko et al. 2020). Additionally, the eastern part of the deformation front contains numerous active thrust faults with fractures that are potentially fluid-filled and therefore sites of high attenuation. Working in Japan, Rietbrock (2001) found low Q_P and high V_P/Vs in the faulted area of the 1995 Kobe earthquake, which exhibits a high density of faults. The high attenuation of these rocks had been attributed to fluid-filled cracks. Eberhart-Phillips (2016) found high attenuation (low Q_P) to be associated with regions of fault zones and microearthquakes in northern California. In New Zealand, regions with high background seismicity also show high attenuation (Eberhart-Phillips et al. 2008), suggesting that small-magnitude earthquakes with only minor slip can generate densely cracked volumes of rock with high permeability and fluid content (Eberhart-Phillips 2016). The weak and damaged zone of earthquakes in the FV region with high fluid-filled cracks can also cause strong attenuation. Some studies showed that fluid content can significantly cause loss of seismic wave energy and trigger earthquake swarms in the upper and lower crust (e.g., Reyners et al. 2007; Mousavi et al. 2017). Our study confirms this by the coincidence of the highly attenuated zone in the FV region with increased earthquake activity (see cross sections A and D of Fig. 7a). In line with these interpretations, we suggest that the prominent high attenuation anomaly in the FV region is caused by the superposition of a dense fault system along the eastern part of the Southern Alpine deformation front and of the fluid-filled sediments in this region, which are also partly affected by faulting.

In contrast, the NWDI shows much lower attenuation at a depth of 10 km (Q_P up to ~ 800, Fig. 6a). At shallower depths, attenuation is slightly higher. However, the characteristic model test (Fig. 5c) showed that the resolution is quite low at depths of 0 and 5 km in this region (most probably due to data coverage). The high Q_P anomaly in the NWDI coincides with higher V_P values (most pronounced at a depth of 10 km, Fig. 6b). The latter has been related to the occurrence of Permian magmatic rocks exposed at the surface (Tadiello and Braitenberg 2021; Jozi Najafabadi et al. 2022). This anomaly also corresponds to a high V_S body at depths between 15 and 40 km, which is regarded as the subsurface prolongation of Permian magmatic rocks (Sadeghi-Bagherabadi et al. 2021). Crystalline rocks have relatively high Q_P and it depends on the rock's physical properties such as porosity and density (Tompkins and Christensen 2001).

As observed in Fig. 6, the NWDI is seismically quiet, with most of the seismic activity concentrated on the boundaries with highly fractured fault zones, namely, along the Southern Alpine deformation front (see above) and at the northern end of the NW–SE Schio–Vicenza strike-slip fault (see e.g., Fig. 6b). The NWDI with low seismicity corresponds roughly to areas with fewer faults and folds at the surface (Castellarin et al. 1987; Schönborn 1999; Castellarin and Cantelli 2000; Reiter et al. 2018), suggesting that these faults are either no longer active or undergoing very slow aseismic slip. The low attenuation values in this area may therefore be attributed partly to sealing of the faults and fractures due to inter- or post-seismic precipitation of secondary minerals from an ancient fluid phase (Gratier and Gueydan 2007). An additional contribution to the low attenuation in this area comes from the prevalence of Permian magmatic rocks (e.g., Castellarin and Cantelli 2000), which are expected to augment the overall strength of the NWDI.

We note that our attenuation images characterize the current state of the subsurface rock masses, rather than the conditions during the northward advancement of the AI in the late Oligocene–Miocene period. Therefore, the highly variable strength of the AI observed today, as inferred from the along-strike variation in Q_P, may differ from its more uniform strength when the AI began advancing northward. Specifically, the NWDI appears to have either maintained or regained high strength since the onset of indentation (as argued above). In contrast, the parts of the AI to the east, in the FV region, have lost strength since the onset of indentation. Their current high attenuation reflects the lower strength of this part of indenter, which is still undergoing folding and faulting, and remains seismically active.

The block of high Q_P crust in the NWDI region is surrounded by lower Q_P areas. Besides the FV region (discussed above), this also holds for the region to the northwest of the NWDI, in which moderate attenuation ($Q_P \sim 300$) can be observed down to ~ 10 km depth (WAU

Jozi Najafabadi *et al. Earth, Planets and Space* (2023) 75:187

Page 12 of 15

in Figs. 6 and 7) between the Engadin Window and the Tauern Window (north of Bolzano). The WAU consists primarily of Paleozoic basement and metamorphosed Mesozoic cover rocks (Schuster and Frank 1999). One would have expected high Q_P values for these predominantly in metamorphic rocks, especially in the uppermost levels of the crust (Handy et al. 2007). We suggest that a high density of fractures and faults in the nappes and the crystalline basement are possible explanations for the moderate Q_P values. In other parts of the Alps, high attenuation was found in crystalline rock bodies which has also been attributed to fractures and shear zones formed during the Alpine orogeny (e.g., Bühnemann and Holliger 1998).

Based on the results and the discussion, we summarize the features of the attenuation tomography as shown in the conceptual model in Fig. 8.

Conclusions

In our study, we introduce a novel model that depicts the 3-D distribution of seismic body P-wave specific attenuation in the subsurface of the Eastern and eastern Southern Alps. To obtain this model, we employed a spectral inversion method to calculate path-average t^* values from the spectral decay of the P-waves which were then inverted by using the simul2000 tomographic code. Through our analysis, we identified several anomalies of

Fig. 8 The conceptual model showing the main anomalies of our study in the tectonic context. The thick gray lines accentuate the PAF and GF lines. The arrow indicates the average direction of the motion of Adria relative to Eurasia (Serpelloni et al. 2016; Devoti et al. 2017). Solid circles depict the earthquakes used in the attenuation tomography and open circles indicate those additionally employed in the travel-time tomography. The dark gray polygons illustrate the surface exposure of Permian magmatic rocks from Tadiello and Braitenberg 2021. High- and low-attenuated anomalies are denoted by red and blue hachured polygons, respectively. For abbreviations see the caption of Fig. 1

both high and low Q_P values, which exhibit correlations with other seismic parameters (e.g., V_P, V_P/V_S and seismicity) and will contribute to the identification of different tectonic and lithological domains:

1) A prominent anomaly characterized by low Q_P, low V_P, and high V_P/V_S is attributed to active deformation along the thrust front of the eastern Southern Alpine. This is interpreted as a domain with a high concentration of fluid-filled faults and fractures. The faulting also affects Plio-Pleistocene sedimentary rocks and unconsolidated sediments along the active thrust front in eastern part of the Southern Alps. The presence of fluids within these sediments is likely responsible for the loss of seismic wave energy, leading to increased attenuation. Indeed, these fluids may potentially contribute to the occurrence of earthquake swarms observed in the area.

2) High Q_P and high V_P, along with moderate V_P/V_S and the general absence of seismicity suggest that the northwestern edge of the Dolomites Sub-Indenter (NWDI) is presently a stronger block compared to its neighboring areas. The eastern part of the Adriatic indenter (AI), which is currently undergoing N–S shortening in response to ongoing Adria-Europe convergence (e.g., Serpelloni et al. 2016), exhibits higher attenuation, in keeping with the occurrence there of seismic faults. Therefore, seismic attenuation can serve as a general proxy for fault activity, as well as an indication of along-strike variability of deformation-induced damage. To the extent that attenuation and damage correlate with rock strength, we infer that the NWDI is currently stronger than the eastern part of the AI. However, we note that the current strength probably differs significantly from the strength of the AI when it was advancing to the north in late Oligocene–Miocene time. Based on the geometry of indentational structures in the Eastern Alps (e.g., Ratschbacher et al. 1991; Rosenberg et al. 2007; Scharf et al. 2013), we infer that the AI was uniformly strong during this time.

3) The occurrence of low-to-moderate Q_P in the western part of the Austroalpine units (WAU), north and west of the Giudicarie fault, can be attributed to widespread fractures and faults in the crystalline basement of that area.
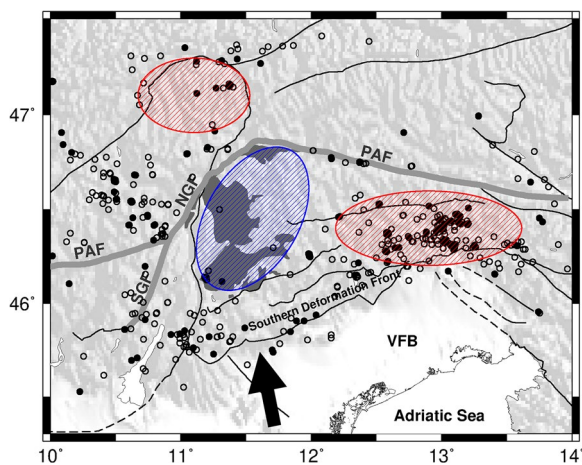
Abbreviations
AASN	AlpArray Seismic Network
AI	Adriatic indenter
FV	Friuli-Venetian
GF	Giudicarie Fault
MRM	Model resolution matrix

NWDI　　Northwestern edge of the Dolomites Sub-Indenter
PF　　Periadriatic Fault
WAU　　Western part of Austroalpine units

Author contributions
All authors contributed to the study conception and design. ANJ performed data preparation and analysis. She also prepared all figures and most of the text. CH supervised the analysis and contributed to the interpretation of the results. ELB and MRH contributed the tectonic interpretation and placed the results in a geological context. MW promoted the work and corrected the text.

Availability of data and materials
The SWATH-D data are available at the GEOFON archive (https://geofon.gfz-potsdam.de; Heit et al. 2017) and the data of the AlpArray Seismic Network (AASN) is available at EIDA (http://www.orfeus-eu.org/data/eida/; Hetényi et al. 2018).

Declarations

Ethics approval and consent to participate
Not applicable.

Consent for publication
Not applicable.

Competing interests
The authors declare that they have no conflict of interest, nor competing interests.

Author details
[1]GFZ German Research Centre for Geosciences, Potsdam, Germany. [2]Institute of Geosciences, Potsdam University, Potsdam, Germany. [3]Institute of Geological Sciences, Freie Universität Berlin, Berlin, Germany.

References
Aki K, Richard PG (1980) Quantities seismology, theory and method. WH. Freeman and Company, New York
Bohm M, Haberland C, Asch G (2013) Imaging fluid-related subduction processes beneath Central Java (Indonesia) using seismic attenuation tomography. Tectonophysics 590:175–188. https://doi.org/10.1016/j.tecto.2013.01.021
Brune JN (1970) Tectonic stress and the spectra of seismic shear waves from earthquakes. J Geophys Res 75:4997–5009. https://doi.org/10.1029/JB075i026p04997
Brune JN (1971) Seismic sources, fault plane studies and tectonics. Eos Trans Am Geophys Union 52:IUGG-178
Bühnemann J, Holliger K (1998) Comparison of high-frequency seismic sources at the Grimsel test site, central Alps, Switzerland. Geophysics 63:1363–1370. https://doi.org/10.1190/1.1444438
Campillo M, Feignier B, Bouchon M, Béthoux N (1993) Attenuation of crustal waves across the Alpine Range. J Geophys Res Solid Earth 98:1987–1996. https://doi.org/10.1029/92JB02357
Castellarin A, Cantelli L (2000) Neo-Alpine evolution of the Southern Eastern Alps. J Geodyn 30:251–274. https://doi.org/10.1016/S0264-3707(99)00036-8
Castellarin A, Fesce AM, Picotti V, Pini GA, Prosser G, Sartori R, Selli L, Cantelli L, Ricci R (1987) Structural and kinematic analysis of the Giudicarie deformation belt. Implications for compressional tectonics of Southern Alps. Mineral Petrogr Acta 30:287–310
Castellarin A, Vai GB, Cantelli L (2006) The Alpine evolution of the Southern Alps around the Giudicarie faults: a Late Cretaceous to Early Eocene transfer zone. Tectonophysics 414:203–223. https://doi.org/10.1016/j.tecto.2005.10.019
Castro RR, Pacor F, Sala A, Petrungaro C (1996) S wave attenuation and site effects in the region of Friuli, Italy. J Geophys Res Solid Earth 101:22355–22369. https://doi.org/10.1029/96JB02295
Devoti R, D'Agostino N, Serpelloni E, Pietrantonio G, Riguzzi F, Avallone A, Cavaliere A, Cheloni D, Cecere G, D'Ambrosio C, Franco L, Selvaggi G, Metois M, Esposito A, Sepe V, Galvani A, Anzidei M (2017) A combined velocity field of the Mediterranean region. Ann Geophys 60:S0215. https://doi.org/10.4401/ag-7059
Eberhart-Phillips D (1986) Three-dimensional velocity structure in northern California Coast Ranges from inversion of local earthquake arrival times. Bull Seismol Soc Am 76:1025–1052. https://doi.org/10.1785/BSSA0760041025
Eberhart-Phillips D (2016) Northern California seismic attenuation: 3D QP and QS models. Bull Seismol Soc Am 106:2558–2573. https://doi.org/10.1785/0120160060
Eberhart-Phillips D, Chadwick M (2002) Seismology-ESE 3-Three-dimensional attenuation model of the shallow Hikurangi subduction zone in the Raukumara Peninsula, New Zealand. J Geophys Res Part B-Solid Earth 107:1. https://doi.org/10.1029/2000JB000046
Eberhart-Phillips D, Michael AJ (1993) Three-dimensional velocity structure, seismicity, and fault structure in the Parkfield Region, central California. J Geophys Res Solid Earth 98:15737–15758. https://doi.org/10.1029/93JB01029
Eberhart-Phillips D, Reyners M, Chadwick M, Stuart G (2008) Three-dimensional attenuation structure of the Hikurangi subduction zone in the central North Island, New Zealand. Geophys J Int 174:418–434. https://doi.org/10.1111/j.1365-246X.2008.03816.x
Evans JR, Eberhart-Phillips D, Thurber CH (1994) User's manual for SIMULPS12 for imaging vp and vp/vs; a derivative of the "Thurber" tomographic inversion SIMUL3 for local earthquakes and explosions
Galadini F, Poli ME, Zanferrari A (2005) Seismogenic sources potentially responsible for earthquakes with M ≥ 6 in the eastern Southern Alps (Thiene-Udine sector, NE Italy). Geophys J Int 161:739–762. https://doi.org/10.1111/j.1365-246X.2005.02571.x
Gentili S, Franceschina G (2011) High frequency attenuation of shear waves in the southeastern Alps and northern Dinarides. Geophys J Int 185:1393–1416. https://doi.org/10.1111/j.1365-246X.2011.05016.x
Gentili S, Gentile G (2015) High frequency attenuation k parameter and Q S 3D model for south-eastern Alps and north-western Dinarides. Boll Geofis Teor Appl 56:383–406
Gratier J-P, Gueydan F (2007) Effect of fracturing and fluid–rock interaction on seismic cycles. In: Handy MR, Hirth G, Hovius N (eds) Tectonic faults: agents of change on a dynamic earth, vol 35. MIT press, Cambridge, p 319e356
Haberland C, Rietbrock A (2001) Attenuation tomography in the western central Andes: a detailed insight into the structure of a magmatic arc. J Geophys Res Solid Earth 106:11151–11167. https://doi.org/10.1029/2000JB900472
Handy MR, Hirth G, Hovius N (2007) Topography, denudation, and deformation. In: Handy MR, Hirth G, Hovius N (eds) Tectonic faults: agents of change on a dynamic earth. MIT Press, Cambridge, pp 205–230
Handy MR, Schmid SM, Bousquet R et al (2010) Reconciling plate-tectonic reconstructions of Alpine Tethys with the geological–geophysical record of spreading and subduction in the Alps. Earth-Sci Rev 102:121–158. https://doi.org/10.1016/j.earscirev.2010.06.002
Handy MR, Ustaszewski K, Kissling E (2015) Reconstructing the Alps–Carpathians–Dinarides as a key to understanding switches in subduction

Jozi Najafabadi *et al. Earth, Planets and Space*   (2023) 75:187

Page 14 of 15

polarity, slab gaps and surface motion. Int J Earth Sci 104:1–26. https://doi.org/10.1007/s00531-014-1060-3

Handy MR, Giese J, Schmid SM et al (2019) Coupled crust-mantle response to slab tearing, bending, and rollback along the Dinaride-Hellenide orogen. Tectonics 38:2803–2828. https://doi.org/10.1029/2019TC005524

Hanks TC, Wyss M (1972) The use of body-wave spectra in the determination of seismic-source parameters. Bull Seismol Soc Am 62:561–589. https://doi.org/10.1785/BSSA0620020561

Hauksson E, Shearer PM (2006) Attenuation models (QP and QS) in three dimensions of the southern California crust: inferred fluid saturation at seismogenic depths. J Geophys Res Solid Earth. https://doi.org/10.1029/2005JB003947

Heit B, Weber M, Tilmann F et al (2017) The Swath-D seismic network in Italy and Austria. GFZ Data Serv. https://doi.org/10.14470/MF7562601148

Heit B, Cristiano L, Haberland C et al (2021) The SWATH-D seismological network in the Eastern Alps. Seismol Res Lett 92:1592–1609. https://doi.org/10.1785/0220200377

Hetényi G, Molinari I, Clinton J et al (2018) The AlpArray seismic network: a large-scale European experiment to image the Alpine Orogen. Surv Geophys 39:1009–1033. https://doi.org/10.1007/s10712-018-9472-4

Hofman LJ, Kummerow J, Cesca S, AlpArray–Swath-D Working Group (2023) A new seismicity catalogue of the eastern Alps using the temporary Swath-D network. Solid Earth 14(10):1053–1066. https://doi.org/10.5194/se-14-1053-2023,2023

Jozi Najafabadi A, Haberland C, Ryberg T et al (2021) Relocation of earthquakes in the southern and eastern Alps (Austria, Italy) recorded by the dense, temporary SWATH-D network using a Markov chain Monte Carlo inversion. Solid Earth 12:1087–1109. https://doi.org/10.5194/se-12-1087-2021

Jozi Najafabadi A, Haberland C, Le Breton E et al (2022) Constraints on crustal structure in the vicinity of the Adriatic indenter (European Alps) from Vp and Vp/Vs local earthquake tomography. J Geophys Res Solid Earth 127:e2021JB023160. https://doi.org/10.1029/2021JB023160

Kissling E, Ellsworth W, Eberhart-Phillips D, Kradolfer U (1994) Initial reference models in local earthquake tomography. J Geophys Res Solid Earth 99:19635–19646

Lanza F, Diehl T, Eberhart-Phillips D et al (2021) 3-D Qp and Qs Seismic Attenuation for the Central Alps and their Foreland. EGU General Assembly 2021 EGU21-8028

Le Breton E, Brune S, Ustaszewski K et al (2021) Kinematics and extent of the Piemont-Liguria Basin—implications for subduction processes in the Alps. Solid Earth 12:885–913. https://doi.org/10.5194/se-12-885-2021

Li Q, Wilcock WSD, Pratt TL et al (2006) Seismic attenuation structure of the Seattle Basin, Washington State, from explosive-source refraction data. Bull Seismol Soc Am 96:553–571. https://doi.org/10.1785/0120040164

Lin G, Shearer PM, Amelung F, Okubo PG (2015) Seismic tomography of compressional wave attenuation structure for Kīlauea Volcano, Hawai'i. J Geophys Res Solid Earth 120:2510–2524

Mavko G, Mukerji T, Dvorkin J (2020) The rock physics handbook. Cambridge University Press, Cambridge

Mayor J, Calvet M, Margerin L et al (2016) Crustal structure of the Alps as seen by attenuation tomography. Earth Planet Sci Lett 439:71–80. https://doi.org/10.1016/j.epsl.2016.01.025

Morasca P, Massa M, Laprocina E et al (2010) Improved 2-D attenuation analysis for Northern Italy using a merged dataset from selected regional seismic networks. J Seismol 14:727–738. https://doi.org/10.1007/s10950-010-9194-7

Mousavi S, Haberland C, Bauer K et al (2017) Attenuation tomography in West Bohemia/Vogtland. Tectonophysics 695:64–75. https://doi.org/10.1016/j.tecto.2016.12.010

Muksin U, Haberland C, Bauer K, Weber M (2013) Three-dimensional upper crustal structure of the geothermal system in Tarutung (North Sumatra, Indonesia) revealed by seismic attenuation tomography. Geophys J Int 195:2037–2049. https://doi.org/10.1093/gji/ggt383

Nussbaum C (2000) Neogene tectonics and thermal maturity of sediments of the easternmost southern Alps (Friuli area, Italy). Ph.D. thesis, Université de Neuchâtel, Switzerland, p 172

Park J, Lindberg CR, Vernon FL III (1987) Multitaper spectral analysis of high-frequency seismograms. J Geophys Res Solid Earth 92:12675–12684. https://doi.org/10.1029/JB092iB12p12675

Peacock S, McCann C, Sothcott J, Astin TR (1994) Experimental measurements of seismic attenuation in microfractured sedimentary rock. Geophysics 59:1342–1351. https://doi.org/10.1190/1.1443693

Pomella H, Klötzli U, Scholger R et al (2011) The Northern Giudicarie and the Meran-Mauls fault (Alps, Northern Italy) in the light of new paleomagnetic and geochronological data from boudinaged Eo-/Oligocene tonalites. Int J Earth Sci 100:1827–1850. https://doi.org/10.1007/s00531-010-0612-4

Pomella H, Stipp M, Fügenschuh B (2012) Thermochronological record of thrusting and strike-slip faulting along the Giudicarie fault system (Alps, Northern Italy). Tectonophysics 579:118–130. https://doi.org/10.1016/j.tecto.2012.04.015

Ratschbacher L, Frisch W, Linzer HG, Merle O (1991) Lateral extrusion in the eastern Alps, Part 2: structural analysis. Tectonics 10(2):257–271. https://doi.org/10.1029/90TC02623

Reiter F, Freudenthaler C, Hausmann H et al (2018) Active seismotectonic deformation in front of the Dolomites indenter, Eastern Alps. Tectonics 37:4625–4654. https://doi.org/10.1029/2017TC004867

Reyners M, Eberhart-Phillips D, Stuart G (2007) The role of fluids in lower-crustal earthquakes near continental rifts. Nature 446:1075–1078. https://doi.org/10.1038/nature05743

Rietbrock A (2001) P wave attenuation structure in the fault area of the 1995 Kobe earthquake. J Geophys Res Solid Earth 106:4141–4154. https://doi.org/10.1029/2000JB900234

Romano MA, Peruzza L, Garbin M, Priolo E, Picotti V (2019) Microseismic Portrait of the Montello Thrust (Southeastern Alps, Italy) from a Dense High-Quality Seismic Network. Seismol Res Lett 90:1502–1517. https://doi.org/10.1785/0220180387

Rosenberg CL, Brun JP, Cagnard F, Gapais D (2007) Oblique indentation in the Eastern Alps: Insights from laboratory experiments. Tectonics 26:2. https://doi.org/10.1029/2006TC001960

Sadeghi-Bagherabadi A, Vuan A, Aoudia A, Parolai S, The AlpArray and AlpArray-Swath Working Groups (2021) High-resolution crustal S-wave velocity model and Moho geometry beneath the Southeastern Alps: new insights from the SWATH-D experiment. Front Earth Sci 9:641113. https://doi.org/10.3389/feart.2021.641113

Sánchez L, Völksen C, Sokolov A et al (2018) Present-day surface deformation of the Alpine region inferred from geodetic techniques. Earth Syst Sci Data 10:1503–1526. https://doi.org/10.5194/essd-10-1503-2018

Sanders C, Iyer H, Hirahara K (1993) Local earthquake tomography: attenuation theory and results. In: Iyer H, Hirahara K (eds) Seismic tomography: theory and practice. Chapman and Hall, New York, pp 676–694

Scharf A, Handy MR, Favaro S, Schmid SM, Bertrand A (2013) Modes of orogen-parallel stretching and extensional exhumation in response to microplate indentation and roll-back subduction (Tauern Window, Eastern Alps). Int J Earth Sci 102(6):1627–1654. https://doi.org/10.1007/s00531-013-0894-4

Scherbaum F (1990) Combined inversion for the three-dimensional Q structure and source parameters using microearthquake spectra. J Geophys Res Solid Earth 95:12423–12438. https://doi.org/10.1029/JB095iB08p12423

Schmid S, Aebli H, Heller F, Zingg A (1989) The role of the Periadriatic Line in the tectonic evolution of the Alps. Geol Soci 45:153–171

Schmid SM, Fügenschuh B, Kissling E, Schuster R (2004) Tectonic map and overall architecture of the Alpine orogen. Eclogae Geol Helv 97:93–117. https://doi.org/10.1007/s00015-004-1113-x

Schmid SM, Bernoulli D, Fügenschuh B et al (2008) The Alpine-Carpathian-Dinaridic orogenic system: correlation and evolution of tectonic units. Swiss J Geosci 101:139–183. https://doi.org/10.1007/s00015-008-1247-3

Schönborn G (1999) Balancing cross sections with kinematic constraints: the Dolomites (northern Italy). Tectonics 18:527–545. https://doi.org/10.1029/1998TC900018

Schuster R, Frank S (1999) Metamorphic evolution of the Austroalpine units east of the Tauern Window: Indications for Jurassic strike slip tectonics. Mitt Ges Geol Bergbaustud Österr 42:37–56

Serpelloni E, Vannucci G, Anderlini L, Bennett RA (2016) Kinematics, seismotectonics and seismic potential of the eastern sector of the European Alps from GPS and seismic deformation data. Tectonophysics 688:157–181. https://doi.org/10.1016/j.tecto.2016.09.026

Slejko D (2018) What science remains of the 1976 Friuli earthquake? Boll Geofis Teor Appl 59:327–350

Tadiello D, Braitenberg C (2021) Gravity modeling of the Alpine lithosphere affected by magmatism based on seismic tomography. Solid Earth 12:539–561. https://doi.org/10.5194/se-12-539-2021

Thurber CH (1983) Earthquake locations and three-dimensional crustal structure in the Coyote Lake Area, central California. J Geophys Res Solid Earth 88:8226–8236. https://doi.org/10.1029/JB088iB10p08226

Tompkins MJ, Christensen NI (2001) Ultrasonic P- and S-wave attenuation in oceanic basalt. Geophys J Int 145:172–186. https://doi.org/10.1046/j.0956-540x.2001.01354.x

Toomey DR, Foulger GR (1989) Tomographic inversion of local earthquake data from the Hengill-Grensdalur Central Volcano Complex, Iceland. J Geophys Res Solid Earth 94:17497–17510. https://doi.org/10.1029/JB094iB12p17497

Um J, Thurber C (1987) A fast algorithm for two-point seismic ray tracing. Bull Seismol Soc Am 77:972–986. https://doi.org/10.1785/BSSA0770030972

Verwater VF, Le Breton E, Handy MR et al (2021) Neogene kinematics of the Giudicarie Belt and eastern Southern Alpine orogenic front (northern Italy). Solid Earth 12:1309–1334. https://doi.org/10.5194/se-12-1309-2021

Wang Z, Zhao D, Liu X et al (2017) P and S wave attenuation tomography of the Japan subduction zone. Geochem Geophys Geosyst 18:1688–1710. https://doi.org/10.1002/2017GC006800

Wessel P, Smith WHF (1991) Free software helps map and display data. EOS Trans Am Geophys Union 72:441–446. https://doi.org/10.1029/90EO00319

Wessel P, Luis JF, Uieda L et al (2019) The generic mapping tools version 6. Geochem Geophys Geosyst 20:5556–5564. https://doi.org/10.1029/2019GC008515

Publisher's Note

Springer Nature remains neutral with regard to jurisdictional claims in published maps and institutional affiliations.